

SUPPLEMENTARY MATERIALS

DEEP LEARNING CELL IMAGING THROUGH ANDERSON LOCALIZING OPTICAL FIBER

JIAN ZHAO,^{1,*} YANGYANG SUN,¹ HONGBO ZHU,² ZHEYUAN ZHU,¹ JOSE E. ANTONIO-LOPEZ,¹ RODRIGO AMEZCUA CORREA,¹ SHUO PANG¹ AND AXEL SCHÜLZGEN¹

¹ CREOL, The College of Optics & Photonics, University of Central Florida, Orlando, FL 32816, USA

² State Key Laboratory of Luminescence and Applications, Changchun Institute of Optics, Fine Mechanics and Physics, Chinese Academy of Sciences, Changchun 130033, China

*Corresponding author: JianZhao@knights.ucf.edu

1. Imaging of multiple cell types

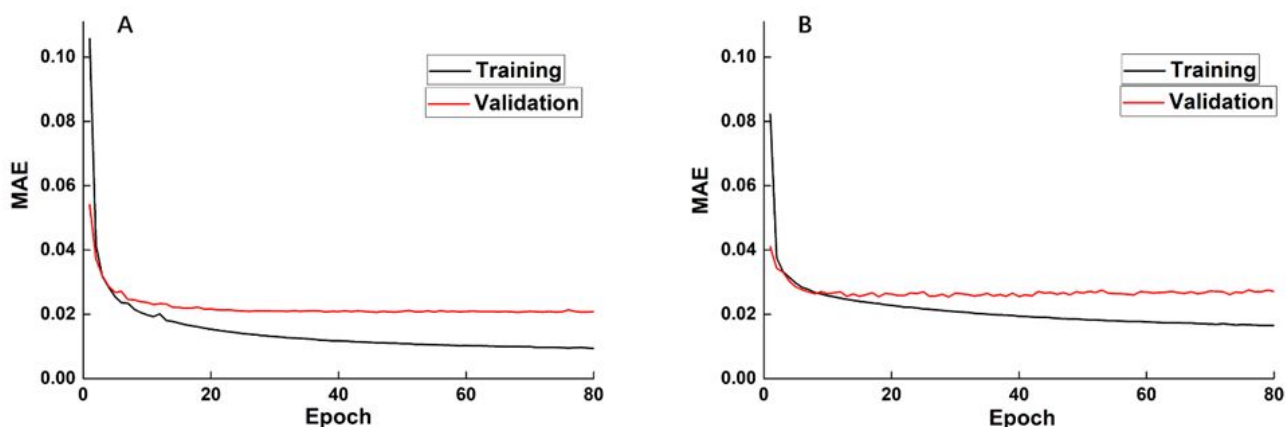


Fig. S1. Accuracy improvement curves during the training process. (A) shows the accuracy improvement curves for training and validation using imaging data of human red blood cells; (B) shows the accuracy improvement curves for training and validation using imaging data of cancerous human stomach cells.

2. Cell imaging at various depth

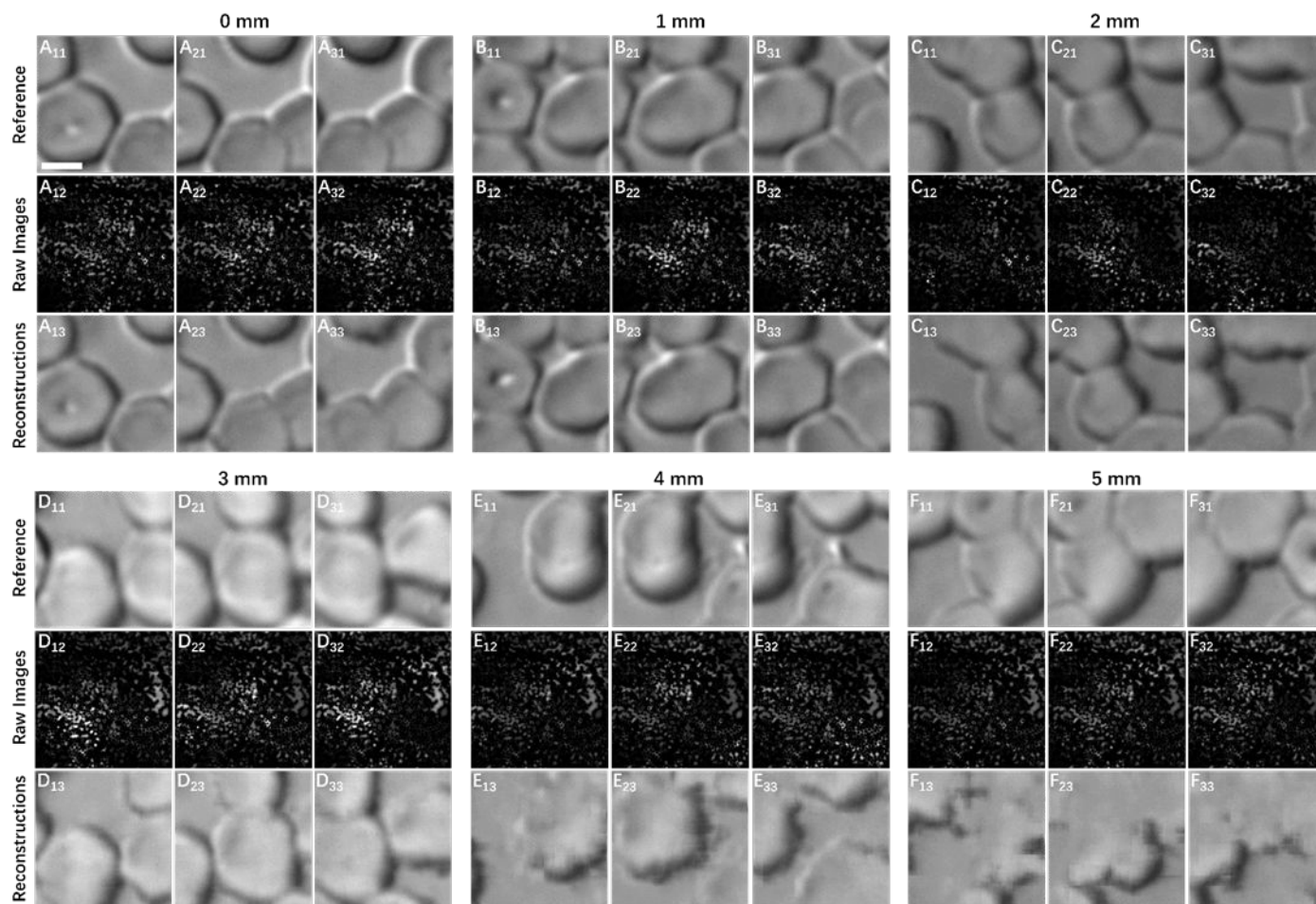


Fig. S2. Multiple depth cell imaging. (A)-(F) shows continuously-scanned sample images of human red blood cells (reference images, raw images transported by the GALOF, and corresponding reconstructed images) recorded at various imaging depths, ranging from 0 mm to 5 mm with a step of 1 mm. The length of the scale bar in (A₁₁) is 4 μ m.

3. Cell imaging with temperature variation and fiber bending

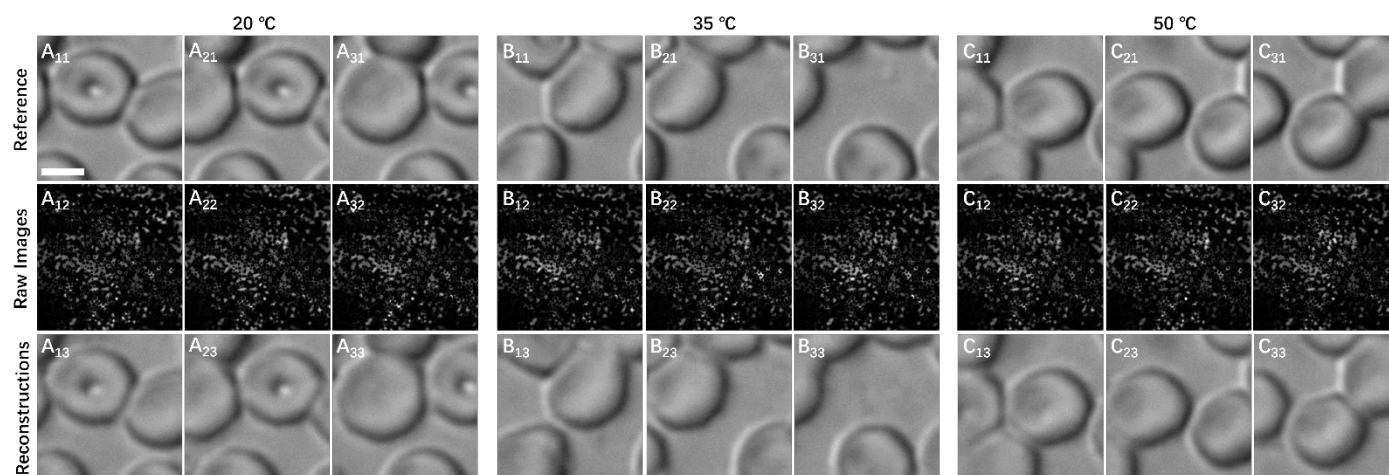


Fig. S3. Cell imaging at different temperature. (A)-(C) shows continuously-scanned sample images human red blood cells (reference images, raw images transported by the GALOF, and corresponding reconstructed images) recorded at three different temperatures of the 10 mm-long heated GALOF segment, ranging from 20 °C to 50 °C. The length of the scale bar in (A₁₁) is 4 μ m.

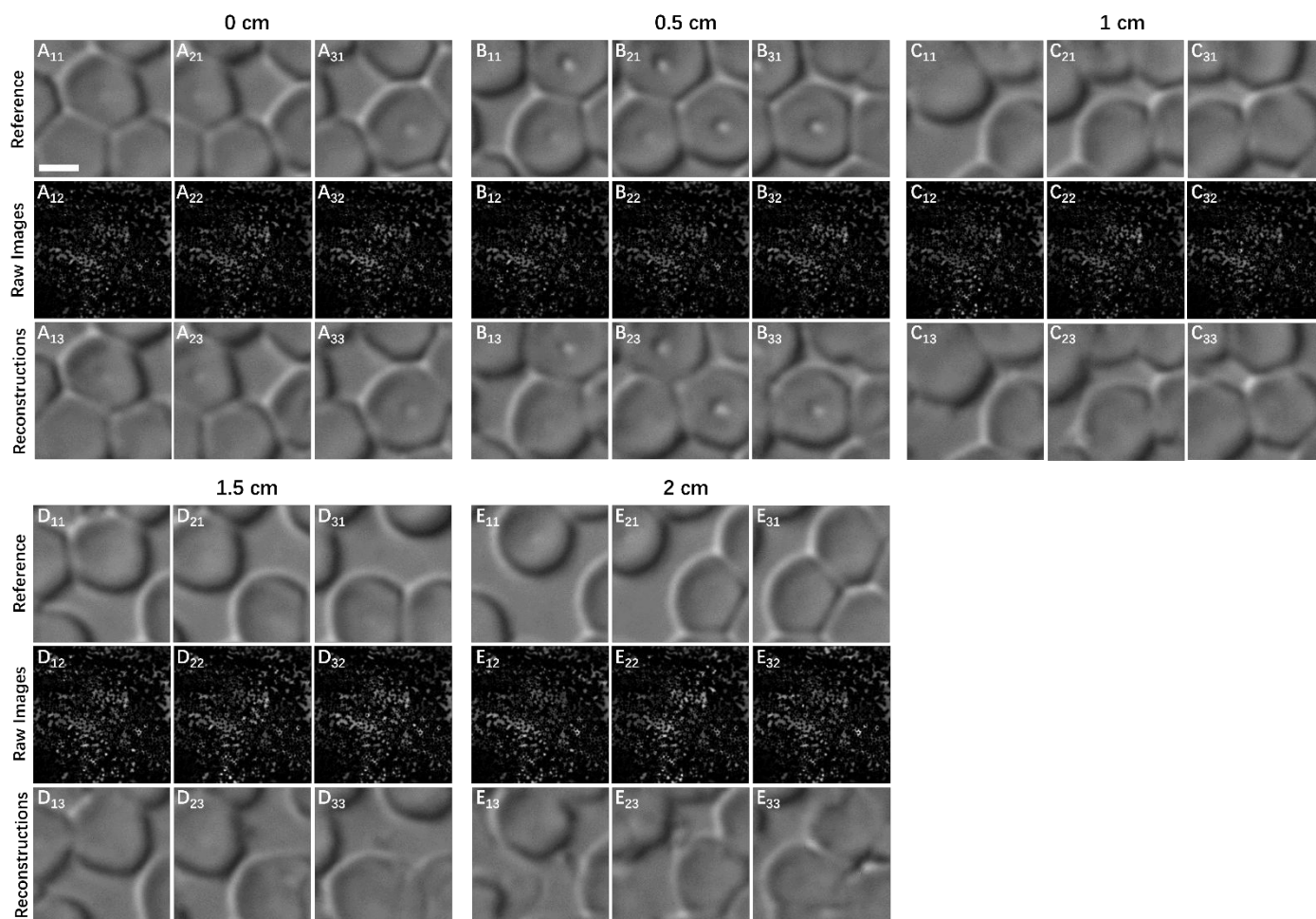


Fig. S4. Cell imaging under bending. (A)-(E) shows continuously-scanned sample images of human red blood cells (reference images, raw images transported by the GALOF, and corresponding reconstructed images) recorded at five different bending offset distances. The definition of the offset distance is illustrated in Fig. 1 (B). An offset distance of 2 cm corresponds to a bending angle of about 3 degrees, see Materials and Methods. The length of the scale bar in (A₁₁) is 4 μm .

4. Average GALOF numerical aperture (NA) estimation

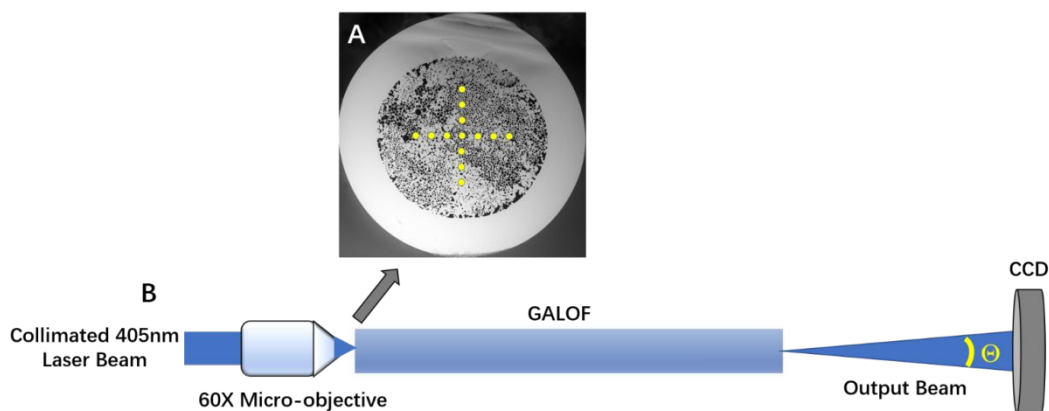


Fig. S5. Far-field emission angle measurement. (A) Yellow dots stand for 13 different coupling locations in the cross-section of the GALOF input facet. The distance between neighboring positions is 10 μm . (B) Experimental setup. A collimated laser beam with a wavelength of 405 nm is coupled to the GALOF input facet using a 60X micro-objective. For each coupling position, the far-field beam is recorded by a CCD camera at various distances from the GALOF exit facet to measure the respective far-field emission angles. $NA = \sin(\theta/2)$.

As shown in Fig. S5, we measure 13 far-field emission angles from which we obtain an averaged NA value of ~ 0.37 with a standard deviation of 0.005.

5. Visualization of DCNN feature maps

Fig. S6 demonstrates how the trained DCNN extracts the high-dimensional feature map from the test raw images through the down-sampling process and recover the original object through the up-sampling process. Each feature map itself is a three-dimensional matrix ($13 \times 13 \times 256$). In order to visualize the feature map, we align 256 sub-feature maps with a size of 13×13 in a two-dimensional plot. From this visualization of the intermediate layers output it is quite clear that the DCNN extracts different feature maps from different raw images.

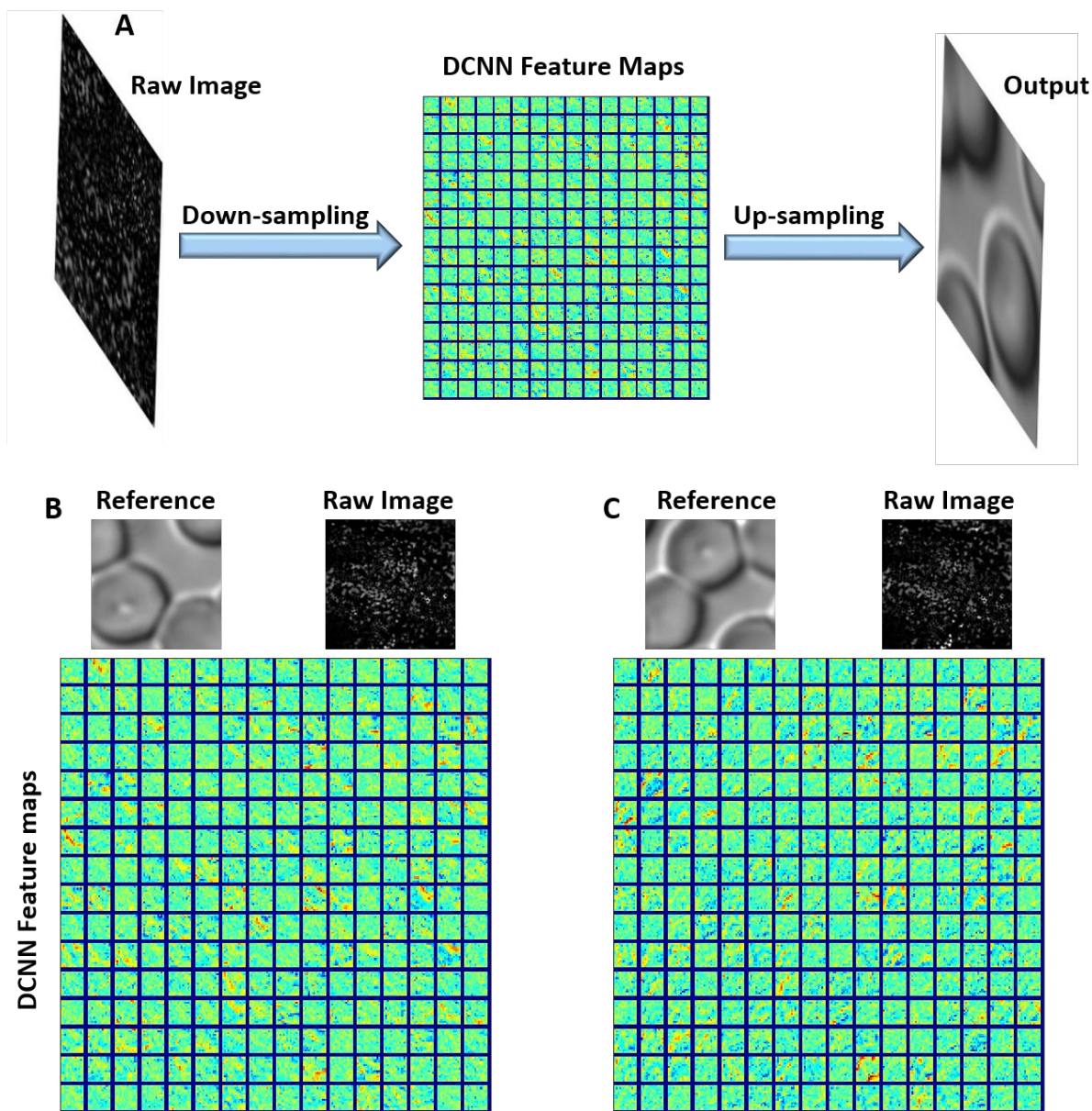


Fig. S6. DCNN feature maps. (A) Schematic of DCNN-based image reconstruction process. (B) and (C) Sample reference and corresponding GALOF-transported raw images of human red blood cells are sent into the trained DCNN to extract their feature maps. The extracted feature maps are plotted by reshaping the three-dimensional data with a size of $13 \times 13 \times 256$ (see Fig. 1 (c)).